IEEE Access
Multidisciplinary | Rapid Review | Open Access Journal

Received April 9, 2020, accepted April 23, 2020, date of publication April 27, 2020, date of current version May 14, 2020.

Digital Object Identifier 10.1109/ACCESS.2020.2990702

Three-Dimensional Scattering From Uniaxial Objects With a Smooth Boundary Using a Multiple Infinitesimal Dipole Method

KAI WANG[1,2], (Member, IEEE), JEAN-JACQUES LAURIN[2], (Senior Member, IEEE), QINGFENG ZHANG[1,3], (Senior Member, IEEE), QINYU ZHANG[1,4], (Senior Member, IEEE), AND KE WU[2], (Fellow, IEEE)

[1]Pengcheng Laboratory, Shenzhen 518000, China
[2]Poly-Grames Research Center, École Polytechnique de Montréal, Montreal, QC H3T 1J4, Canada
[3]Department of Electrical and Electronic Engineering, Southern University of Science and Technology, Shenzhen 518055, China
[4]Communication Engineering Research Centre, Harbin Institute of Technology at Shenzhen, Shenzhen 518055, China

Corresponding author: Kai Wang (kai.wang@polymtl.ca)

This work was supported in part by The Verification Platform of Multi-Tier Coverage Communication Network for Oceans Project under Grant LZC0020, in part by the Natural Sciences and Engineering Research Council (NSERC) of Canada, in part by the Consortium for Aerospace Research and Innovation in Canada (CARIC), in part by the Bombardier Aerospace, in part by the Isoneo Inc., in part by the National Natural Science Foundation of China under Grant 61871207, and in part by the Shenzhen Science and Technology Innovation Committee Funds under Grant JCYJ20190809115419425.

ABSTRACT The formulations for three-dimensional (3D) scattering from uniaxial objects with a smooth boundary using a multiple infinitesimal dipole method (MIDM) are introduced. The proposed technique uses two sets of infinitesimal dipole triplets (IDTs), including three co-located orthogonally polarized electric infinitesimal dipoles, distributed inside and outside of a scatterer to construct simulated fields. The dyadic Green's functions of uniaxial materials are deployed in the MIDM so as to obtain the simulated fields. The singularity issues in using the uniaxial dyadic Green's functions, which cannot be solved analytically so far for a general uniaxial medium, can be easily eliminated by using the proposed MIDM. In comparison to the traditional single-layered distribution scheme of IDTs, the proposed multiple-layered distribution scheme can handle the scattering from uniaxial objects accurately and efficiently. Several numerical examples are presented to study bistatic radar cross section (RCS) responses under different scenarios. Excellent agreement is achieved by comparing numerical results with those obtained from commercial software packages, while the simulation performance including CPU time and required memory is drastically improved by using the MIDM when computing a general uniaxial material or a relatively larger object. The proposed technique has its merits on simplicity, conciseness and fast computation in comparison to existing numerical methods.

INDEX TERMS Multiple infinitesimal dipole method (MIDM), uniaxial materials, scattering, dyadic Green's function, singularities, method of auxiliary sources (MAS).

I. INTRODUCTION

The interaction between electromagnetic waves and anisotropic materials has received a great deal of attentions recently. Anisotropic materials have found a variety of applications in the design of antennas [1]–[7], integrated-circuit structures [8], reduction of RCS of scatterers [9], optical signal processing [10] and so on. One of the basic problems to investigate waves in the anisotropic material is to study the scattering characteristics of an anisotropic object. Several remarkable research contributions have been made and presented in [11]–[23]. The volumetric integral equation (VIE)-based methods were introduced in [11]–[16], [23] to compute scattering performances from an arbitrarily shaped object made of a linear, lossy, and anisotropic material. The VIE-based approaches can handle the most general cases of materials whereas they require to discretize the entire volume of an object, therefore becoming computationally challenging with large scatterers. The same issue will also rise in the finite-difference time domain (FDTD) [19], [22]

The associate editor coordinating the review of this manuscript and approving it for publication was Su Yan.

and finite element-boundary integral (FE-BI) [20] methods. The surface integral equation (SIE) is a good candidate to overcome the computational burden of the methods based on volumetric discretization. A SIE-based MoM scheme combined with uniaxial dyadic Green's functions [24], [25] was proposed in [17], [18] for scattering evaluation from arbitrarily shaped objects filled with electrically uniaxial materials. The SIE-based solutions provide an accurate and more simplified approach compared to the VIE-based ones, yet the complexity of formulations is still there. The proposed analytical approach in [17] for eliminating singularity issues is only valid for an electrically uniaxial material, and it would fail when a general uniaxial material is encountered.

The generalized multipole technique (GMT) [26], [27] is a generic name of several similar numerical methods [28]–[31] developed independently by several research groups. In the GMT, the scattered fields are usually expanded in terms of a set of multipole sources. However, not only the multipoles can be used for fields expansion, but other equivalent sources are also possible. Therefore, other names for similar methodologies have been given like multiple multipole method (MMP) [28], discrete sources method (DSM) [29], method of auxiliary sources (MAS) [30], or multifilament current model (MFCM) [31]. A common basic concept of all these methods is that the scattered fields inside and outside of a scatterer are simulated by a set of equivalent sources respectively located outside and inside of the scatterer with a certain distance away from the physical boundary, rather than being formulated in terms of equivalent surface currents flowing on the physical surface. In this case, no integrals have to be computed numerically which reduces the computation time and simplifies the problem formulation. Also the solution features no singularity. So far, most of the scattering problems tackled with the GMT have considered isotropic objects, and there is few research work on the anisotropic scenario. In [32], the GMT was extended to anisotropic scatterers by introducing the plane wave representation of an anisotropic material into Bessel multipoles, but it resulted in integrals which cannot be evaluated analytically to represent the scattered fields. The DSM was extended to three-dimensional anisotropic scatterers in [33], but the entire body of the scatterer needed to be discretized. As a result, DSM also suffers from a high computational burden as in the case of the VIE-based method when larger objects are involved. Recently, the random auxiliary sources (RAS) method, a MMP-inspired numerical technique, was introduced in [34]–[36]. But all applications of the RAS currently only focused on isotropic materials. To the best of the authors′ knowledge, there is no research reported to date about combining the GMT-like methods with dyadic Green's functions of anisotropic materials to study the scattering from anisotropic objects.

The uniaxial material seems to be the most widely used type of anisotropic materials. This is because the uniaxial material can be either easily found in many natural crystals [8], [37], or artificially made by a stacked dielectric sheet structure consisting of alternative layers of two isotropic materials [4], [5], [38], [39], or obtained by homogenizing a mixture of several different materials via effective medium theory [40], [41]. This work only focuses on the uniaxial material, yet the proposed MIDM can also be applied to other kinds of anisotropic materials as long as the corresponding dyadic Green's functions are available. In the MIDM, the integral operations used in the VIE- or SIE-based methods are avoided. Instead, a simple point-matching testing procedure is used and the harmonics of a multipole source which is used in the MMP are also cast off by deploying the infinitesimal dipole source. Without using the integral operations and the harmonics of the sources, the computation of scattered fields speeds up and the problem formulation is also simplified. However, in comparison with the MMP which uses high order harmonics in equivalent sources, a larger number of infinitesimal dipole sources will be required in the MIDM to represent varying fields. An approach similar to the proposed MIDM is used in [42]. However, only isotropic materials were considered, and the strategy for the placement of sources may fail when a relatively larger object is involved, as will be shown in Section IV.

The scattering from uniaxial objects with a smooth boundary using a MIDM is proposed in this paper. The applications of structures with a smooth boundary can be found in many scenarios, such as the spherical dielectric resonator antennas, lens antennas, extended hemispherical lens antennas and so on. The paper is organized as follow. The formulation of the problem is presented in Section II, where the strategies for placements of matching points and sources that play a key role in the MIDM, will be discussed in detail and specified there. The singularity issues in using uniaxial dyadic Green's functions are discussed and solved in Section III. Several numerical examples are presented in Section IV under different scenarios. All numerical results are compared with simulated results generated from commercial software package, and excellent agreement is obtained. Finally, a conclusion to summarize the proposed technique is given in Section V.

II. FORMULATION OF THE MIDM

The geometry of the problem is illustrated in Fig. 1. Two regions are present, the external region 1 is free space and

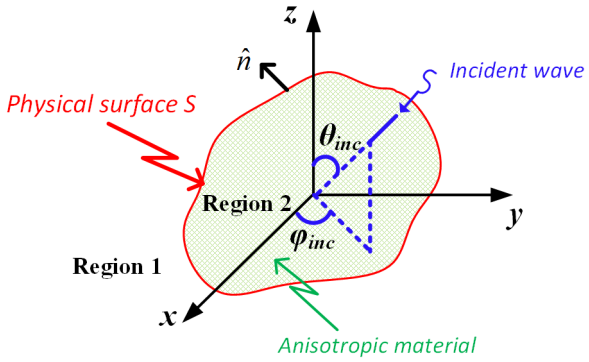

FIGURE 1. Geometry of the problem.

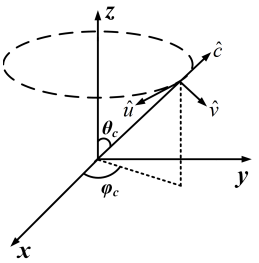

FIGURE 2. The configurations of rotated global and global coordinates.

the internal region 2 is occupied by an homogeneous uniaxial material characterized by

$$\overline{\epsilon} = \begin{pmatrix} \epsilon_1 & 0 & 0 \\ 0 & \epsilon_1 & 0 \\ 0 & 0 & \epsilon_2 \end{pmatrix}_{\hat{u}\hat{v}\hat{c}}, \quad \overline{\mu} = \begin{pmatrix} \mu_1 & 0 & 0 \\ 0 & \mu_1 & 0 \\ 0 & 0 & \mu_2 \end{pmatrix}_{\hat{u}\hat{v}\hat{c}} \tag{1}$$

The rotated global coordinate system, represented by unit vectors $\hat{\boldsymbol{u}}$, $\hat{\boldsymbol{v}}$ and $\hat{\boldsymbol{c}}$ as shown in Fig. 2, are used to express the uniaxial medium. $\hat{\boldsymbol{c}}$ is the unit vector parallel to the optical axis of the medium. ϵ_1, μ_1 and ϵ_2, μ_2 are the permittivity and permeability associated with the directions perpendicular and parallel to the optical axis ($\hat{\boldsymbol{c}}$), respectively. The relationship between the unit vectors in the rotated global and global coordinates is written as

$$\begin{pmatrix} \hat{\boldsymbol{u}} \\ \hat{\boldsymbol{v}} \\ \hat{\boldsymbol{c}} \end{pmatrix} = \begin{pmatrix} \sin\varphi_c & -\cos\varphi_c & 0 \\ \cos\theta_c\cos\varphi_c & \cos\theta_c\sin\varphi_c & -\sin\theta_c \\ \sin\theta_c\cos\varphi_c & \sin\theta_c\sin\varphi_c & \cos\theta_c \end{pmatrix} \begin{pmatrix} \hat{x} \\ \hat{y} \\ \hat{z} \end{pmatrix} \tag{2}$$

where θ_c and φ_c are defined in Fig. 2. The concept of the MIDM is illustrated in Fig. 3. We place a set of infinitesimal dipole triplets (IDTs) in regions 1 and 2. Each IDT contains three co-located orthogonal polarized infinitesimal dipoles, namely point sources. The formulation of the proposed MIDM is conducted through a two-step equivalence. Firstly, the scattered fields in the region 1 are generated by equivalent IDTs placed in the region 2, and those point sources are treated as source currents radiating in unbounded vacuum. Secondly, the internal fields in the region 2 are generated by equivalent IDTs placed in the region 1, and those point sources are radiating in unbounded space filled with an homogeneous uniaxial material identical to that constituting the scatterer.

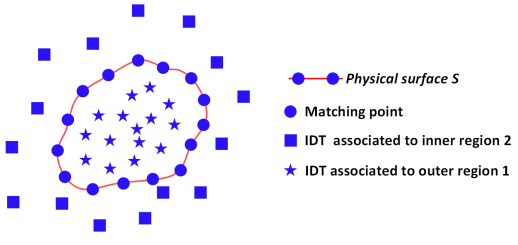

FIGURE 3. The concept of the MIDM.

A. FIELDS EXPRESSIONS IN REGIONS 1 AND 2

Region 1, considered as free space, contains the incident ($\boldsymbol{E_{inc}}, \boldsymbol{H_{inc}}$) and the scattered fields ($\boldsymbol{E_1^s}, \boldsymbol{H_1^s}$). If the incident fields are the plane wave, they could be written as:

$$\boldsymbol{E_{inc}} = \hat{\boldsymbol{p}} e^{-jk(x\sin\theta_{inc}\cos\varphi_{inc} + y\sin\theta_{inc}\sin\varphi_{inc} + z\cos\theta_{inc})} \tag{3a}$$

$$\boldsymbol{H_{inc}} = \frac{1}{\eta_0}\hat{\boldsymbol{k}} \times \boldsymbol{E_{inc}} \tag{3b}$$

where $\hat{\boldsymbol{p}}$ is the polarized direction of the incident electric field, and $\hat{\boldsymbol{k}}$ is the unit vector of the wave vector. The scattered fields could be constructed in a simple manner and expressed in terms of the dyadic Green's functions. So the total fields ($\boldsymbol{E_1}, \boldsymbol{H_1}$) could be expressed as:

$$\boldsymbol{E_1} = \boldsymbol{E_{inc}} + \sum_{i=1}^{N_1} \overline{\boldsymbol{G}}_{\boldsymbol{ee}}^{\boldsymbol{1}}(\boldsymbol{r}, \boldsymbol{r'}) \cdot (\boldsymbol{J}_{\boldsymbol{i1}}^{\boldsymbol{1}}(\boldsymbol{r'}) + \boldsymbol{J}_{\boldsymbol{i2}}^{\boldsymbol{1}}(\boldsymbol{r'}) + \boldsymbol{J}_{\boldsymbol{i3}}^{\boldsymbol{1}}(\boldsymbol{r'})) \tag{4a}$$

$$\boldsymbol{H_1} = \boldsymbol{H_{inc}} + \sum_{i=1}^{N_1} \overline{\boldsymbol{G}}_{\boldsymbol{me}}^{\boldsymbol{1}}(\boldsymbol{r}, \boldsymbol{r'}) \cdot (\boldsymbol{J}_{\boldsymbol{i1}}^{\boldsymbol{1}}(\boldsymbol{r'}) + \boldsymbol{J}_{\boldsymbol{i2}}^{\boldsymbol{1}}(\boldsymbol{r'}) + \boldsymbol{J}_{\boldsymbol{i3}}^{\boldsymbol{1}}(\boldsymbol{r'})) \tag{4b}$$

where $\boldsymbol{J}_{\boldsymbol{i1}}^{\boldsymbol{1}}, \boldsymbol{J}_{\boldsymbol{i2}}^{\boldsymbol{1}}$ and $\boldsymbol{J}_{\boldsymbol{i3}}^{\boldsymbol{1}}$ are the three orthogonal electric point sources in the ith IDT associated to the region 1. Noticing that three magnetic point sources can also be deployed in each IDT, and dyadic Green's functions ($\overline{\boldsymbol{G}}_{\boldsymbol{em}}$ and $\overline{\boldsymbol{G}}_{\boldsymbol{mm}}$) are then required with respect to the magnetic point source. Only electric point source based IDT is utilized throughout this paper. In (4), N_1 is the number of IDTs placed in the region 2. The two Green's functions, $\overline{\boldsymbol{G}}_{\boldsymbol{ee}}^{\boldsymbol{1}}$ and $\overline{\boldsymbol{G}}_{\boldsymbol{me}}^{\boldsymbol{1}}$, in (4) are the dyadic Green's functions of isotropic materials, corresponding to the electric and magnetic fields radiated into the region 1 by an electric point source, which read [25]

$$\overline{\boldsymbol{G}}_{\boldsymbol{ee}}^{\boldsymbol{1}} = -j\omega\mu_0(\overline{\boldsymbol{I}} + \frac{\nabla\nabla}{k^2})\frac{e^{-jkR}}{4\pi R} \tag{5a}$$

$$\overline{\boldsymbol{G}}_{\boldsymbol{me}}^{\boldsymbol{1}} = -(1 + jkR)\frac{e^{-jkR}}{4\pi R^3}(\boldsymbol{R} \times \overline{\boldsymbol{I}}) \tag{5b}$$

with

$$\boldsymbol{R} = \boldsymbol{r} - \boldsymbol{r'}, \quad R = |\boldsymbol{R}|$$

where $\boldsymbol{r'}$ and $\boldsymbol{r}$ are the locations of the source and observation points, respectively. $k = k_0 = \omega\sqrt{\epsilon_0\mu_0}$ is the wavenumber of free space herein. The term $\overline{\boldsymbol{I}}$ is the identity dyad defined in global coordinates.

The region 2 only contains the internal fields generated by the IDTs placed outside of it, and the expressions of fields read

$$\boldsymbol{E_2} = \sum_{i=1}^{N_2} \overline{\boldsymbol{G}}_{\boldsymbol{ee}}^{\boldsymbol{2}}(\boldsymbol{r}, \boldsymbol{r'}) \cdot (\boldsymbol{J}_{\boldsymbol{i1}}^{\boldsymbol{2}}(\boldsymbol{r'}) + \boldsymbol{J}_{\boldsymbol{i2}}^{\boldsymbol{2}}(\boldsymbol{r'}) + \boldsymbol{J}_{\boldsymbol{i3}}^{\boldsymbol{2}}(\boldsymbol{r'})) \tag{6a}$$

$$\boldsymbol{H_2} = \sum_{i=1}^{N_2} \overline{\boldsymbol{G}}_{\boldsymbol{me}}^{\boldsymbol{2}}(\boldsymbol{r}, \boldsymbol{r'}) \cdot (\boldsymbol{J}_{\boldsymbol{i1}}^{\boldsymbol{2}}(\boldsymbol{r'}) + \boldsymbol{J}_{\boldsymbol{i2}}^{\boldsymbol{2}}(\boldsymbol{r'}) + \boldsymbol{J}_{\boldsymbol{i3}}^{\boldsymbol{2}}(\boldsymbol{r'})) \tag{6b}$$

where $\boldsymbol{J}_{\boldsymbol{i1}}^{\boldsymbol{2}}, \boldsymbol{J}_{\boldsymbol{i2}}^{\boldsymbol{2}}$ and $\boldsymbol{J}_{\boldsymbol{i3}}^{\boldsymbol{2}}$ are the three orthogonal electric point sources in the ith IDT associated to the region 2. N_2 is the

number of IDTs placed in the region 1. Since region 2 is occupied by the uniaxial material, the two Green's functions, $\overline{\boldsymbol{G}}_{ee}^{\boldsymbol{2}}$ and $\overline{\boldsymbol{G}}_{me}^{\boldsymbol{2}}$, in (6) are the uniaxial dyadic Green's functions, corresponding to the electric and magnetic fields radiated into the region 2 by an electric point source, which read [24], [25]

$$\overline{\boldsymbol{G}}_{ee}^{\boldsymbol{2}} = -j\omega\mu_1(\epsilon_2\overline{\boldsymbol{\epsilon}}^{-1} + \frac{\nabla\nabla}{k_u^2})g_e + j\omega\mu_1\overline{\boldsymbol{T}} \tag{7a}$$

$$\begin{aligned}\overline{\boldsymbol{G}}_{me}^{\boldsymbol{2}} &= (g_e - g_m)(\boldsymbol{R}\cdot\hat{\boldsymbol{c}})\frac{[\hat{\boldsymbol{c}}\times\boldsymbol{R_c}]\boldsymbol{R_c} + \boldsymbol{R_c}[\hat{\boldsymbol{c}}\times\boldsymbol{R_c}]}{|\boldsymbol{R_c}|^4} \\ &+ \frac{(1+jk_uR_e)\epsilon_2 g_e}{\epsilon_1 R_e^2}\frac{\boldsymbol{R_c}[\boldsymbol{R}\times\boldsymbol{R_c}]}{|\boldsymbol{R_c}|^2} \\ &- \frac{(1+jk_uR_m)\mu_2 g_m}{\mu_1 R_m^2}\frac{[\boldsymbol{R}\times\boldsymbol{R_c}]\boldsymbol{R_c}}{|\boldsymbol{R_c}|^2}\end{aligned} \tag{7b}$$

with

$$\begin{aligned}&k_u = \omega\sqrt{\epsilon_1\mu_1}, \quad \boldsymbol{R_c} = \boldsymbol{R}\times\hat{\boldsymbol{c}} \\ &g_e = \frac{e^{-jk_uR_e}}{4\pi R_e}, \quad g_m = \frac{e^{-jk_uR_m}}{4\pi R_m} \\ &R_e = \sqrt{\epsilon_2\boldsymbol{R}\cdot\overline{\boldsymbol{\epsilon}}^{-1}\cdot\boldsymbol{R}}, \quad R_m = \sqrt{\mu_2\boldsymbol{R}\cdot\overline{\boldsymbol{\mu}}^{-1}\cdot\boldsymbol{R}} \\ &\overline{\boldsymbol{T}} = (\frac{\epsilon_2}{\epsilon_1}g_e - \frac{\mu_2}{\mu_1}g_m)\frac{\boldsymbol{R_c}\boldsymbol{R_c}}{|\boldsymbol{R_c}|^2} \\ &\quad +(\hat{u}\hat{u} + \hat{v}\hat{v} - \frac{2\boldsymbol{R_c}\boldsymbol{R_c}}{|\boldsymbol{R_c}|^2})\frac{j(R_eg_e - R_mg_m)}{k_u|\boldsymbol{R_c}|^2}\end{aligned}$$

B. PLACEMENT OF MATCHING POINTS

The matching points should be distributed as uniform as possible in order to capture the behavior of fields on the physical surface of a scatterer with a smooth boundary. A simple and efficient way to place matching points is to make use of the Rao-Wilton-Glisson(RWG)-mesh [43] information which can be exported from commercial software package FEKO [44]. As shown in Fig. 4, the locations of nodes constituting a RWG-mesh are used to place the matching points. The parameter, TEL(triangle edge length) defined in FEKO, is used to control the density of a generated RWG-mesh. In the MIDM, we firstly model the investigated object in FEKO and then run the mesh module to generate a RWG-mesh. The matching points are followed to be placed with the help of nodes information of exported RWG-mesh, and a uniform placement can be finally achieved easily. The total number of matching points, N_m, is determined by the TEL value defined in FEKO.

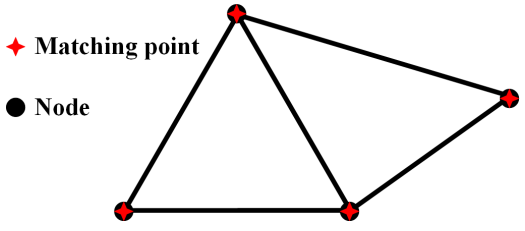

FIGURE 4. Placement of matching points by using a RWG-mesh.

C. PLACEMENT OF IDTs

The IDTs are placed inside and outside of an object to construct the simulated fields outside and inside, respectively. A multiple-layered sources distribution scheme is proposed for the placement of IDTs in this paper. L virtual surfaces, which have the identical shape with the physical surface, are formed by scaling the physical surface to internal and external regions. L scale parameters are linearly spaced in the range $0.2 \sim 0.995$ for internal and $1.5 \sim 2.5$ for external regions based on empirical experiments. For the single-layered distribution, $L = 1$, the scale parameters are 0.2 and 2.0 for internal and external regions as found in [42]. A total number of IDTs (N_s) are unequally allocated to the L layers, and the number of IDTs in each layer is determined with respect to ratios between L scale parameters. The larger scale parameter corresponds to more IDTs. The placement of IDTs also makes use of the nodes information of a RWG-mesh generated by FEKO. Once the number of IDTs for ith layer, N_{si}, is obtained, we select N_{si} points from N_m nodes orderly, and transform those nodes to internal and external regions using the scale parameter of the ith layer. Finally, a multiple-layered distribution scheme of IDTs is realized. An illustrative example of three-layered IDTs distribution strategy is shown in Fig. 5.

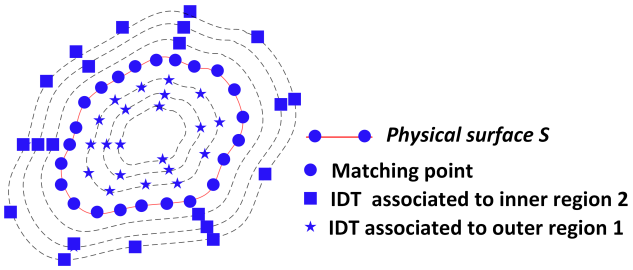

FIGURE 5. An illustrative example of three-layered placement of IDTs.

D. BOUNDARY CONDITIONS

The connection between the fields in regions 1 and 2 is dictated by the boundary conditions of surface S shown in Fig. 1. Specifically, the tangential components of electric and magnetic fields must be continuous along the physical boundary S, which leads to

$$\begin{aligned}\hat{\boldsymbol{n}}\times\boldsymbol{E}_1 &= \hat{\boldsymbol{n}}\times\boldsymbol{E}_2 \\ \hat{\boldsymbol{n}}\times\boldsymbol{H}_1 &= \hat{\boldsymbol{n}}\times\boldsymbol{H}_2\end{aligned} \tag{8}$$

where $\hat{\boldsymbol{n}}$ is a unit vector normal to the closed smooth surface S as shown in Fig. 1. A matrix is then created by imposing the boundary condition at a number of matching points on S. Two tangential electric and magnetic fields are calculated at each matching point, therefore the formulated matrix has $4N_m$ rows. On the other hand, $2N_s$ IDTs in two regions are used to simulate the tangential fields, and therefore $6N_s$ infinitesimal electric dipoles are deployed in the simulation resulting in a matrix with $6N_s$ columns. The number of matching

points (N_m) must therefore satisfy the inequality

$$N_m \geq 1.5N_s \tag{9}$$

in order to have a unique soloution for the unknown current coefficients.

Upon the application of a point-matching procedure, we will finally obtain a matrix expression of the type

$$[Q]\boldsymbol{X} = \boldsymbol{B} \tag{10}$$

where $\boldsymbol{X}$ is a column vector containing the unknown dipole coefficients, and $\boldsymbol{B}$ is another column vector containing samples of incident tangential fields at the matching points. $[Q]$ is a matrix whose entries are obtained from the tangential fields of IDTs at matching points, and it could be rectangular or square depending on whether oversampling is used or not. If it is in a square form, a unique solution can be found, otherwise the smallest least-square error solution is pursued and known to be

$$\boldsymbol{X} = (\left[\tilde{Q}\right]^* [Q])^{-1} \left[\tilde{Q}\right]^* \boldsymbol{B} \tag{11}$$

where $\left[\tilde{Q}\right]$ is the transpose of $[Q]$ and the asterisk denotes complex conjugate.

E. CONVERGENCE STUDY

In order to study the convergence of results, we make use of the error on the imposed tangential boundary conditions as a metric, whose definitions read

$$\Delta E_{bc} = \frac{|\hat{n} \times (\boldsymbol{E}_1^s + \boldsymbol{E}_{inc} - \boldsymbol{E}_2)|}{|\boldsymbol{E}_{inc}|} \tag{12a}$$

$$\Delta H_{bc} = \frac{|\hat{n} \times (\boldsymbol{H}_1^s + \boldsymbol{H}_{inc} - \boldsymbol{H}_2)|}{|\boldsymbol{H}_{inc}|} \tag{12b}$$

where ΔE_{bc} and ΔH_{bc} are evaluated on a more dense points than the matching points selected on the physical surface S. The necessary numbers of sources and matching points in the MIDM are increased until ΔE_{bc} and ΔH_{bc} reach the desired level of accuracy.

III. SINGULARITIES IN USING DYADIC GREEN's FUNCTIONS

Two types of singularity issues usually appear when using the dyadic Green's functions. The first singularity issue is involved in both free space and uniaxial dyadic Green's functions when $|\boldsymbol{R}|$, the distance between source and matching points, is approaching zero. A special treatment on this issue should be considered in the SIE-based solution whereas this type of singularity is completely avoided in our case because the sources are placed at a certain distance away from the matching points. The other singularity appears in the usage of the uniaxial dyadic Green's functions when the term $|\boldsymbol{R_c}|$ vanishes, which means $\boldsymbol{R}$ is parallel to the optical axis $\hat{\boldsymbol{c}}$, and $\boldsymbol{R_c}/|\boldsymbol{R_c}|$ becomes undefined as can be seen from (7). A special treatment on this issue has been proposed in [17] for the SIE-based methodology. However, that treatment is only valid for an electrically uniaxial object and should also valid for an magnetically uniaxial object according to the duality theorem. For a general uniaxial material, the proposed solution in [17] is not applicable. Moreover, up to authors' knowledge, the analytical solution for the second type of singularity of a general uniaxial material has not been reported so far.

Instead of deriving complex analytical solutions, a quite simple approach to eliminate the second singularity issue by removing the problematic sources is proposed in our proposed method. Once the locations of matching points and sources are generated as specified in Sec. II-B and II-C, we implement a filtering strategy to find those locations of sources letting $\boldsymbol{R}$ to be parallel to $\hat{\boldsymbol{c}}$ with a criterion $|\boldsymbol{R_c}| \leqslant 1e^{-5}$. Those detected problematic sources are removed directly in the MIDM in order to avoid the second type of singularity issue. It was found that the number of problematic sources is much less than the total number of sources, therefore it is safe to remove them without scarifying the accuracy. This strategy has been found to be a quite efficient way to handle the second singularity issue in our numerical examples.

IV. NUMERICAL EXAMPLES AND OTHER DISCUSSIONS

Based on the numerical scheme described in the previous sections, a computer program has been implemented. The program computes the normalized bistatic radar cross section (RCS) (σ/λ^2) in *xoz* and *yoz* planes, defined as

$$\frac{\sigma}{\lambda^2} = \lim_{r\to\infty}(4\pi r^2 \frac{|E^s|^2}{\lambda^2 \left|E^i\right|^2}) \tag{13}$$

where $\boldsymbol{E^s}$ is the total scattered electric field in the region 1, and λ is the incident wavelength.

The MIDM procedure flowchart is shown in Fig. 6, and the initial value of TEL is defined regarding to the electric size of an investigated scatterer. For a 3D object, it is better to set the initial TEL value as 0.08 if the volume of the scatterer is within $(2\lambda)^3$, and the initial TEL value is better to be set as 0.16 if the volume of the scatterer is between $(2\lambda)^3$ and $(4\lambda)^3$ based on the empirical experiences. When the volume is larger than $(4\lambda)^3$, unfortunately, it is impossible for us give the initial value of TEL because the CST

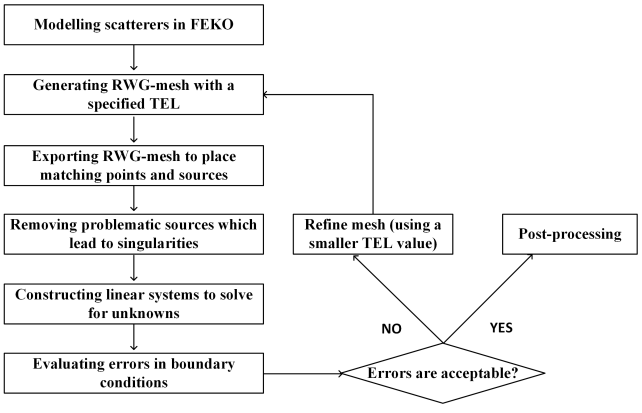

FIGURE 6. The flowchart of the proposed MIDM.

installed on the server we can access encounters a stagnation in the simulation and hard to generate simulation results. The step of the refine mesh operation in Fig. 6 is set as 0.01 to regenerate a RWG-mesh in FEKO. We use $L = 4$ for the multilayered distribution of sources in four illustrative examples, and the layer number factor will be analyzed and discussed later. The computed results are compared with the reference results obtained from commercial software package CST where 4 cells per wavelength for the model and the background is set in the mesh properties of CST.

A. FOUR ILLUSTRATIVE EXAMPLES

The first example is a both electrically and magnetically uniaxial sphere with radius $r_a = 0.5\lambda$ illuminated by a plane wave with an unit magnitude of $\hat{\boldsymbol{x}}$ polarized electric field and propagating along the z axis. The uniaxial medium parameters are $\epsilon_1 = 2\epsilon_0$, $\epsilon_2 = 4\epsilon_0$, $\mu_1 = 3\mu_0$, $\mu_2 = 5\mu_0$ and the optical axis $\hat{\boldsymbol{c}}$ is parallel to the z axis. The normalized bistatic RCS responses in *xoz* and *yoz* planes are shown in Fig. 7(a) and 7(b). The computed results are compared with simulation results obtained from commercial software CST [45] where the finite-element method (FEM) is applied. Good agreement can be observed between the MIDM using single-layered ($L = 1$) or four-layered ($L = 4$) distribution scheme and CST. To further quantify the performance of the proposed MIDM, the relative difference, as defined in (14), between the normalized bistatic RCS responses obtained from the MIDM with $L = 1$ or $L = 4$ sources distributions and CST is evaluated.

$$Error(dB) = |RCS(MIDM) - RCS(CST)| \tag{14}$$

The relative difference responses of the first numerical example are shown in Fig. 8(a) and 8(ab). Apart from a big difference appeared around $\theta = 90°$ in *yoz* plane, the relative difference responses are small for the MIDM with $L = 1$ or $L = 4$ as observed in Fig. 8, which corresponds to the good agreement presented in Fig. 7. It is reasonable to have a big difference appeared around $\theta = 90°$ in Fig. 8(b) because the relative difference is evaluated at the peak values of simulated results obtained from MIDM and CST.

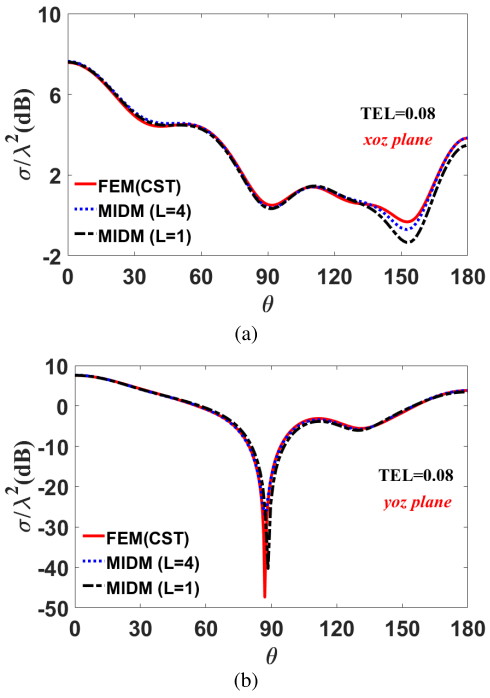

FIGURE 7. Normalized bistatic RCS responses of a uniaxial sphere illuminated by a plane wave with $\hat{x}$ polarized electric field propagating along the z axis in (a) *xoz* plane and (b) *yoz* plane. ($r_a = 0.5\lambda$, $\epsilon_1 = 2\epsilon_0, \epsilon_2 = 4\epsilon_0, \mu_1 = 3\mu_0, \mu_2 = 5\mu_0, \theta_c = 0°$).

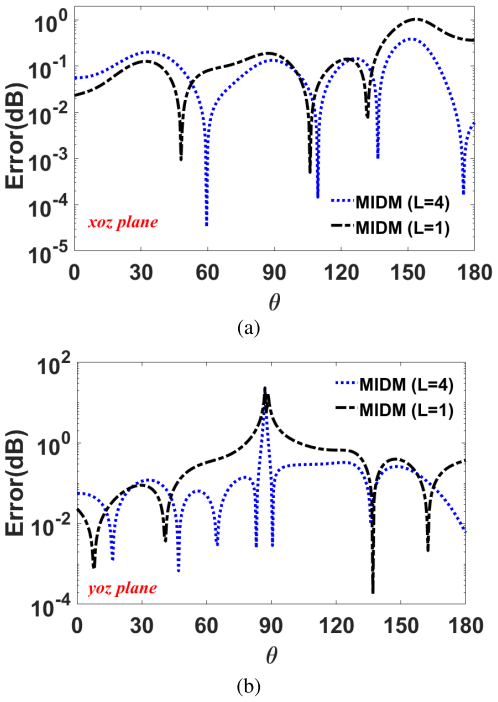

FIGURE 8. The relative differences in *xoz* and *yoz* planes of the computed normalized RCS responses between the MIDM and CST for the first numerical example.

The second example is related to an electrically uniaxial capsule with a height $h = \lambda$ and two end-capped hemispheres with a radius $r_a = 0.5\lambda$, as shown in Fig. 9(a), illuminated by a plane wave with an unit magnitude of $\hat{\boldsymbol{x}}$ polarized electric field and propagating along $-z$ axis. The uniaxial medium parameters are $\epsilon_1 = 5\epsilon_0$, $\epsilon_2 = 9\epsilon_0$, $\mu_1 = \mu_2 = \mu_0$ and the orientation of $\hat{\boldsymbol{c}}$ is defined as $\theta_c = 45°$ and $\varphi_c = 90°$. The computed normalized RCS results in *xoz* and *yoz* planes of two IDTs distribution strategies are shown in Fig. 9, and are compared with those obtained from CST. For the single-layer scheme, which is referred from [42], a disagreement on the normalized RCS computation is obvious to see, yet the proposed multilayered distribution strategy with $L = 4$ works well and excellent agreement is observed. This phenomenon is also indicated by the relative difference responses in *xoz* and *yoz* planes as shown in Fig. 10, where a small difference is observed for the $L = 4$ sources distribution scheme whereas

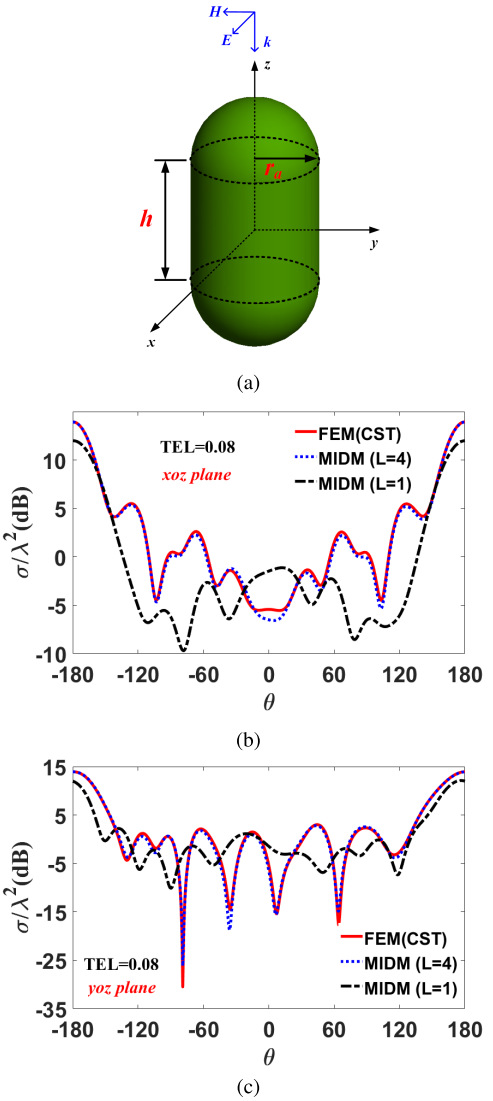

FIGURE 9. (a) A uniaxial capsule with a height $h = \lambda$ and two end-capped hemispheres with a radius $r_a = 0.5\lambda$ illuminated by a plane wave with $\hat{x}$ polarized electric field propagating along the $-z$ axis. Normalized bistatic RCS responses in (b) *xoz* plane and (c) *yoz* plane. ($\epsilon_1 = 5\epsilon_0, \epsilon_2 = 9\epsilon_0, \mu_1 = \mu_2 = \mu_0, \theta_c = 45°, \varphi_c = 90°$).

a large difference is obtained for the $L = 1$ counterpart. Since the axis $\hat{\boldsymbol{c}}$ is oriented in the *yoz* plane, the scattered field pattern in the *yoz* plane will be asymmetric as observed in Fig. 9(c).

Another different shape of scatterer is considered in the third example where six offset spheres merged. Six spheres are identical with a radius $r_a = 0.5\lambda$, and are placed by offsetting one's center to six axes with a distance $0.5r_a$, as shown in Fig. 11(a). The uniaxial medium parameters are $\epsilon_1 = 2\epsilon_0$, $\epsilon_2 = 8\epsilon_0$, $\mu_1 = 3\mu_0$, $\mu_2 = 9\mu_0$, therefore a relative large ratio of anisotropy is considered, and the optical axis $\hat{\boldsymbol{c}}$ is parallel to the z axis. This scatterer is illuminated by a plane wave with an unit magnitude of $\hat{\boldsymbol{x}}$ polarized electric field and propagating along z axis, as shown in Fig. 11(a). The normalized RCS results are computed in both *xoz* and *yoz*

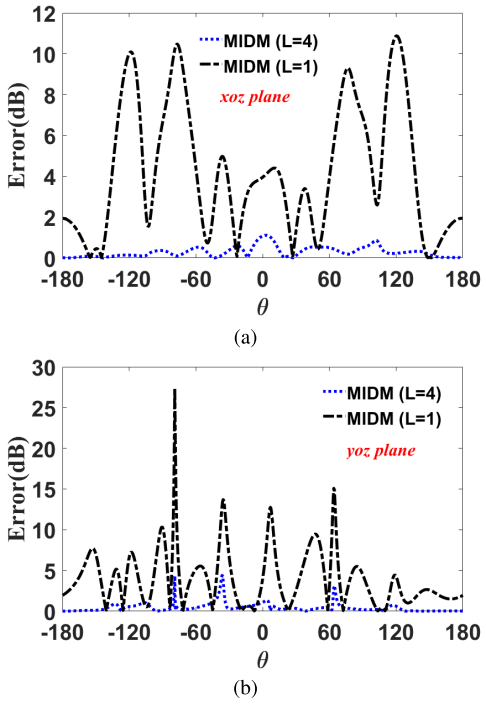

FIGURE 10. The relative differences in *xoz* and *yoz* planes of the computed normalized RCS responses between the MIDM and CST for the second numerical example.

planes with single- and multiple-layered IDTs distribution schemes, and are compared with results obtained from CST as shown in Fig. 11. Once again, the single-layered scheme fails to have a good agreement on the normalized RCS simulation with that from commercial software package, whereas the proposed multilayered IDTs distribution scheme can. This also coincides with the results presented in Fig. 12 where a large difference is observed for the MIDM with $L = 1$ and a small difference is achieved when the multilayered sources distribution scheme is deployed in the MIDM.

The last example is about scattering from a uniaxial layer coated PEC sphere as shown in Fig. 13. In Comparison to previous three examples, three regions instead of two are presented in this scenario. The outermost region 1 is free space, the region 2 is a layer occupied with an anisotropic T_iO_2 material, and the innermost region 3 is a PEC sphere with a radius r_a. The medium parameters of T_iO_2 are $\epsilon_1 = 5.913\epsilon_0$, $\epsilon_2 = 7.197\epsilon_0$, $\mu_1 = \mu_2 = \mu_0$ as referred from [46], and $r_b = 2r_a = 0.6\lambda$. The incident plane wave has a unit magnitude of $\hat{\boldsymbol{x}}$ polarized electric field and propagating along z axis. The formulation is similar to previous examples. The only difference is that additional sources located within the region 3 are required to simulate the fields inside of the anisotropic layer, as shown in Fig. 13(b). It is noteworthy that the locations of sources in Fig. 13(b) are randomly depicted to illustrate the concept of MIDM, and the practical implementation of sources placements is referred to Sec. II-C. The simulated normalized RCS responses are presented in Fig. 14. Since the electric size of this example is relatively small, both

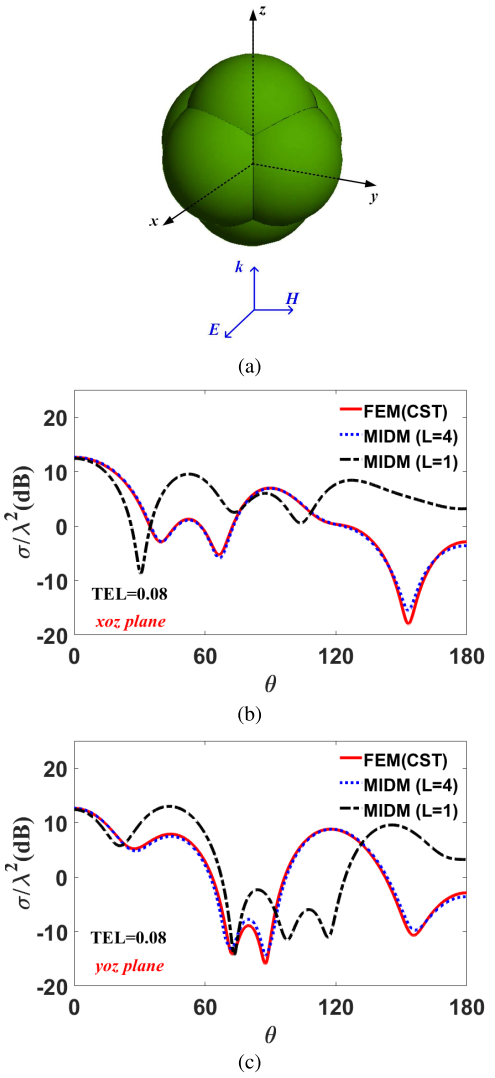

FIGURE 11. (a) Six offset spheres-merged structure illuminated by a plane wave with an unit magnitude of $\hat{x}$ polarized electric field and propagating along z axis. Normalized bistatic RCS responses in (b) *xoz* plane and (c) *yoz* plane. ($\epsilon_1 = 2\epsilon_0, \epsilon_2 = 8\epsilon_0, \mu_1 = 3\mu_0, \mu_2 = 9\mu_0, \theta_c = 0°$).

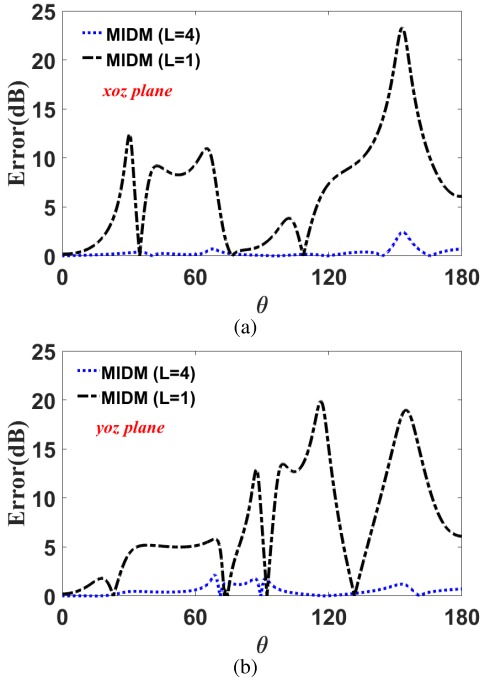

FIGURE 12. The relative differences in *xoz* and *yoz* planes of the computed normalized RCS responses between the MIDM and CST for the third numerical example.

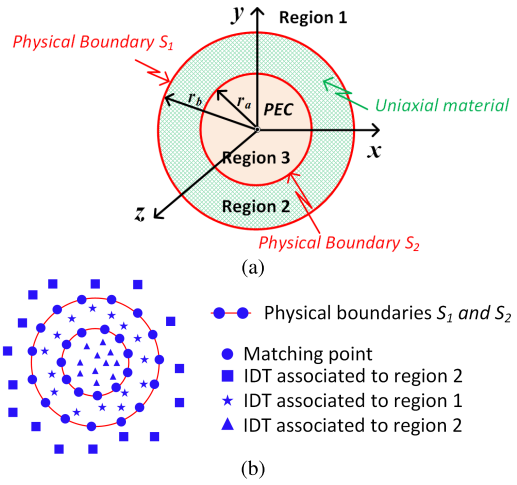

FIGURE 13. (a)Geometry of and (b)the concept of MIDM for a PEC sphere coated with a T_iO_2 layer.

$L = 4$ and $L = 1$ sources distributions in MIDM can generate normalized RCS results which have good agreement with that obtained from the CST. The relative difference responses of the two sources distributions are also small as presented in Fig. 15.

B. SINGULARITY ISSUE AND SIMULATION PERFORMANCES

The TEL value is set as 0.08 in FEKO to generate a RWG-mesh for placements of matching points and IDTs in three numerical examples. The resulting numbers of matching points (N_m) and IDTs (N_s) for each example are displayed in Table 1. As discussed in Sec. III, two types of singularity issues are encountered in using the dyadic Green's functions as discussed in [17]. The first type of singularity issue is not existing in the proposed MIDM, but the second type of singularity occurs. With the help of the freedom of sources placement in MIDM, a filtering strategy can be easily implemented to find those problematic sources as introduced in Sec. III. The number of problematic sources (N_{sp}) detected under the criterion $|\boldsymbol{R_c}| \leqslant 1e^{-5}$ in each numerical example is presented in Table 1. Specifically, in the fourth numerical example, the RWG-mesh generated by FEKO results in 854 and 218 matching points on physical boundaries S_1 and S_2, respectively, and the numbers of IDTs are 569 for regions 1 and 2, and 145 for the innermost region 3. The numbers of problematic sources are 6 in region 1 and 4 in

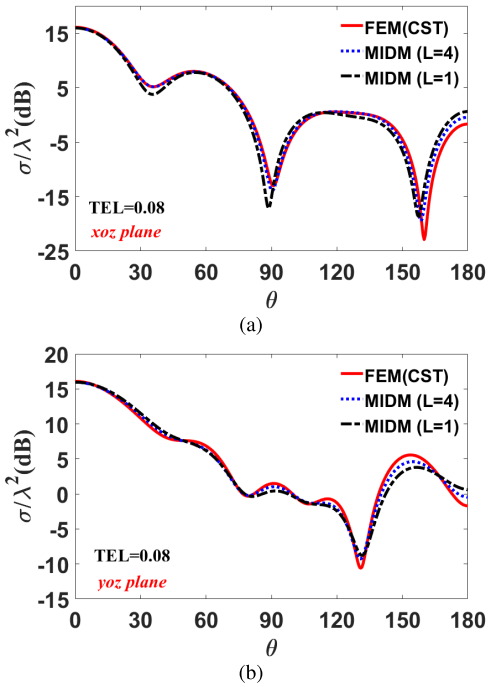

FIGURE 14. Normalized bistatic RCS responses in (a) *xoz* plane and (b) *yoz* plane for a T_iO_2 layer coated PEC sphere illuminated by a plane wave with an unit magnitude of $\hat{x}$ polarized electric field and propagating along z axis. ($r_b = 2r_a = 0.6\lambda$, $\epsilon_1 = 5.913\epsilon_0$, $\epsilon_2 = 7.197\epsilon_0$, $\mu_1 = \mu_2 = \mu_0$, $\theta_c = 0°$, $\varphi_c = 180°$).

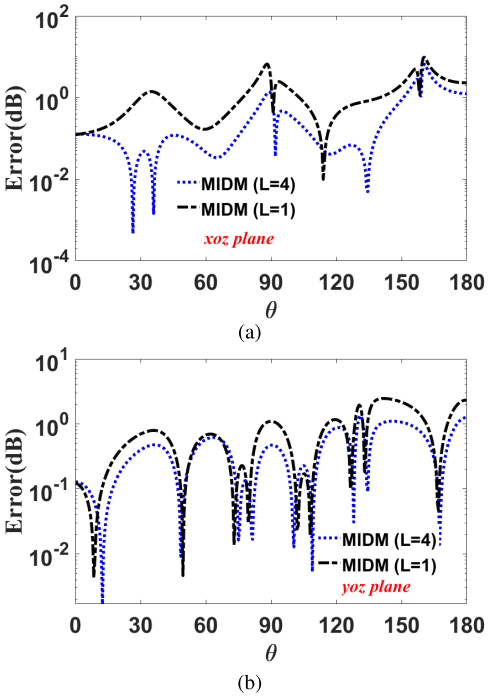

FIGURE 15. The relative differences in *xoz* and *yoz* planes of the computed normalized RCS responses between the MIDM and CST for the fourth numerical example.

region 3 for single-layered sources distribution scheme, and are 4 in region 1 and 3 in region 3 for the fourth-layered one. Since the number of problematic sources is much less than the total number of sources, it is therefore safe to directly remove them in the MIDM resulting a singularity free numerical solution in simulating uniaxial materials.

TABLE 1. The numbers of matching points (N_m) and IDTs (N_s) with respect to the TEL value and the number of problematic IDTs (N_{sp}) in each illustrative example.

	TEL	N_m	N_s	$N_{sp}(L=1)$	$N_{sp}(L=4)$
Eg.1	0.08	596	397	4	3
Eg.2	0.08	1176	784	0	0
Eg.3	0.08	1109	739	2	2
Eg.4	0.08	854+218	569+145	6+4	4+3

TABLE 2. The comparisons of CPU time (s) and memory (GB) between the proposed method and commercial software CST.(The simulations of examples 1, 2 and 4 were run on the desk computer with an Intel(R) Core(TM) i7-7700@3.6 GHz, and of example 3 were run on the server with an Intel(R) Xeon(R) E5-2680@2.70 GHz).

	CST(FEM)		MIDM($L=4$)	
	CPU time	Memory	CPU time	Memory
Eg.1	147	2.27	84	0.08
Eg.2	196	2.43	440	0.33
Eg.3	29584	145.06	1192	0.29
Eg.4	360	5.97	265	0.22

The simulation performance including the CPU time and the required memory of the proposed MIDM and commercial software CST is displayed in Table 2. The cost on the required memory is drastically reduced by using the MIDM in comparison to the FEM-based solver of CST. This is because a surface discretization method is deployed in MIDM whereas the volume discretization strategy is utilized in the FEM-based solver of CST. It is noteworthy to mention that the surface discretization-based method for simulating anisotropic materials has yet been incorporated in any commercial software so far. Except for the second example, the CPU time by using the proposed MIDM is also smaller than that used in CST, and the simulation performance has more distinct advantages by using the proposed MIDM if a relatively larger scatterer is encountered, as will be introduced in Sec. IV-C. It is noteworthy that our programs are written in MATLAB [47] and we authors are not professional programmer. It is expected that the performance of the MIDM can be improved if a compiled programming language is utilized.

C. LAYER NUMBERS AND BOUNDARY CONDITION ERROR RESPONSES

The four-layered sources distribution scheme has been proven to be feasible for the simulation of uniaxial objects with a smooth boundary and better than the single-layered one in previous examples. Yet $L = 4$ is a special case, it is therefore necessary to investigate the MIDM with different layer numbers in order to validate the feasibility of multiple-layered scheme. We then study a T_iO_2 sphere with a radius $r_a = 2\lambda$ illuminated by a plane wave with an unit magnitude of $\hat{\boldsymbol{x}}$ polarized electric field and propagating along z axis. The TEL is set as 0.16 in FEKO to generate a

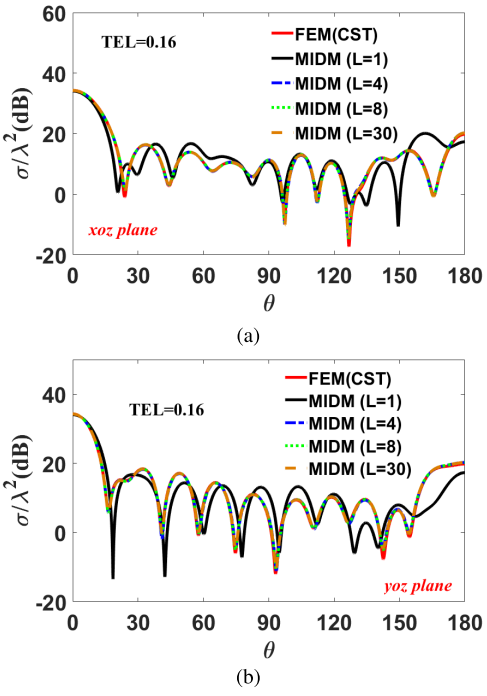

FIGURE 16. Normalized bistatic RCS responses of a T_iO_2 sphere illuminated by a plane wave with $\hat{x}$ polarized electric field propagating along the z axis in (a) *xoz* plane and (b) *yoz* plane with different layer numbers. ($r_a = 2\lambda$, $\epsilon_1 = 5.913\epsilon_0$, $\epsilon_2 = 7.197\epsilon_0$, $\mu_1 = \mu_2 = \mu_0$, $\theta_c = 0°$, $\varphi_c = 180°$).

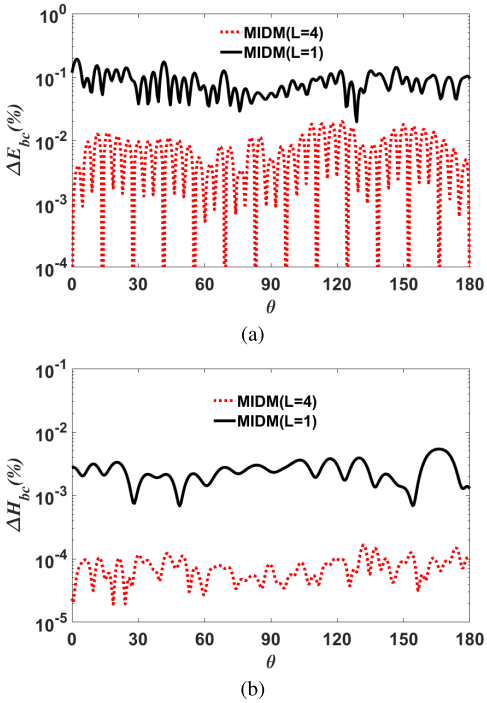

FIGURE 17. The (a) electric and (b) magnetic boundary condition error responses of a T_iO_2 sphere by using different sources distribution schemes. ($r_a = 2\lambda$, $\epsilon_1 = 5.913\epsilon_0$, $\epsilon_2 = 7.197\epsilon_0$, $\mu_1 = \mu_2 = \mu_0$, $\theta_c = 0°$, $\varphi_c = 180°$).

RWG-mesh for placements of matching points and sources, and resulting 2346 mathcing points and 1564 IDTs. The normalized RCS results are computed in both *xoz* and *yoz* planes under different layer numbers of sources, and are presented in Fig. 16. The number of problematic IDTs is much less the total number of IDTs for each different layer number scenario, and is omitted herein. The results generated by using $L = 4$, $L = 8$ and $L = 30$ are almost the same and have excellent agreement with that obtained from CST, whereas the signle-layered scheme fails to provide an accurate solution.

To further study this phenomenon, we turn to evaluate the boundary condition error response, which is a straightforward way to examine the accuracy of the solution. The tangential electric and magnetic field boundary condition errors, as defined in (12), in the *xoz* plane for single-layered and four-layered distribution schemes of IDTs are presented in Fig. 17. It can be observed that the multilayered scheme, $L = 4$, possesses a better response in ΔE_{bc} or ΔH_{bc}, which means a solution with a higher accuracy can be obtained if the multiple-layered strategy is deployed in the MIDM. By considering the inaccurate responses generated by the single-layered scheme as shown in Fig. 16, a boundary condition error criterion is therefore required to be set. The criterion $(\Delta E_{bc} \& \Delta H_{bc}) \leq 0.1\%$ is used in judging the acceptance of errors in MIDM procedure as shown in Fig. 6 to make sure the computed results are accurate. The simulations of the T_iO_2 sphere problem were run on a large memory (384 GB) installed server with an Intel(R) Xeon(R) E5-2680@2.70 GHz, and the CPU time and required memory for the proposed MIDM are 8811 s and 1.31 GB, respectively, whereas for commercial software package CST are 82980 s and 170.20 GB, respectively. Obvioulsy, the simulation performance has been drastically improved by using the proposed MIDM.

V. CONCLUSIONS AND DISCUSSIONS

The MIDM, an efficient momentum solution, has been introduced, formulated and further utilized in the three-dimensional scattering computation of uniaxial scatterers with a smooth boundary in this work. The uniaxial dyadic Green's functions have been deployed in the GMT-like method, namely the proposed MIDM, for the first time. A simple and efficient strategy to avoid the second type of singularity issue, which cannot be analytically solved so far for a general uniaxial medium, is proposed. The placements of matching points and sources, which play a key role in the MIDM, have been discussed and specified in detail by making use of the RWG-mesh generated by FEKO. The proposed multiple-layered distribution scheme of sources has been proven to be feasible and accurate in the scattering simulation from a relatively larger objects in comparison to the traditional single-layered counterpart. Several numerical examples are investigated under different scenarios, such as shapes of scatterers, electrical sizes of scatterers, and material characteristics, and the computed results of the proposed MIDM with a multiple-layered sources distribution scheme for each example have excellent agreement with simulated results obtained from commercial software package CST.

The cost on required memory has been drastically reduced by using the proposed MIDM, and the CPU time of simulation in the MIDM is also better than that in CST when a general uniaxial material or a relatively larger scatterer is considered. Only uniaxial materials have been investigated in this paper, yet the MIDM can also handle certain types of anisotropic materials, such as chiral, isotropic warm plasma and bi-isotropic materials, since their closed-form Green's functions are available [25]. Although the anisotropic materials with an arbitrary full tensor permittivity and permeability or with a general inhomogeneous configuration which can be handled by the volume discretization-based methods are highly impossible to be tackled by the surface discretization-based methods, for example the proposed MIDM, the proposed technique has shown a significant advantage on the simulation performance in this work when a homogeneous general uniaxial material is considered, and this advantage is definitely inherited in electromagnetic computations of other anisotropic materials whose closed-form dyadic Green's functions are reachable by using the proposed MIDM.

The limitation of the proposed MIDM appears in simulating an object with sharp corners. The fast variation of fields near the corner requires more matching points and sources to be placed around the corner in order to better approximate the behavior of fields there, as discussed in [35], [48], [49] where a two-dimensional scenario was discussed. In this case, the proposed methodology may fail to apply. To overcome this drawback, an adaptive mesh strategy by applying a fine mesh around the corner and a standard mesh on other areas should be deployed, and a strategy to place more sources around the sharp corner is also required in the MDIM. Another alternative solution could be found in [36] where a RWG-mesh based testing method and a randomly distribution scheme of infinitesimal dipoles are deployed, and scatterers involving sharp corners has been successfully simulated by using the RAS method. The electromagnetic simulation of an anisotropic scatterer with sharp corners by using the MIDM would be our future work and will be presented in the future publications.

ACKNOWLEDGMENT

The authors would like to thank the European H-2020 EPICEA consortium for insightful discussions.

REFERENCES

[1] D. Pozar, "Radiation and scattering from a microstrip patch on a uniaxial substrate," *IEEE Trans. Antennas Propag.*, vol. 35, no. 6, pp. 613–621, Jun. 1987.

[2] T.-W. Kim, J.-S. Park, and S.-O. Park, "A theoretical model for resonant frequency and radiation pattern on rectangular microstrip patch antenna on liquid crystal substrate," *IEEE Trans. Antennas Propag.*, vol. 66, no. 9, pp. 4533–4540, Sep. 2018.

[3] P. Kopyt, B. Salski, P. Zagrajek, D. Obrebski, and J. Marczewski, "Modeling of silicon-based substrates of patch antennas operating in the sub-THz range," *IEEE Trans. THz Sci. Technol.*, vol. 7, no. 4, pp. 424–432, Jul. 2017.

[4] S. Fakhte, H. Oraizi, and L. Matekovits, "High gain rectangular dielectric resonator antenna using uniaxial material at fundamental mode," *IEEE Trans. Antennas Propag.*, vol. 65, no. 1, pp. 342–347, Jan. 2017.

[5] S. Fakhte, H. Oraizi, L. Matekovits, and G. Dassano, "Cylindrical anisotropic dielectric resonator antenna with improved gain," *IEEE Trans. Antennas Propag.*, vol. 65, no. 3, pp. 1404–1409, Mar. 2017.

[6] A. Bostani and H. Oraizi, "Analysis and design of tapered uniaxial-anisotropic dielectric rod antennas," *IEEE Trans. Antennas Propag.*, vol. 65, no. 11, pp. 5787–5795, Nov. 2017.

[7] A. Mehdipour, T. A. Denidni, A.-R. Sebak, and C. W. Trueman, "Reconfigurable TX/RX antenna systems loaded by anisotropic conductive carbon-fiber composite materials," *IEEE Trans. Antennas Propag.*, vol. 62, no. 2, pp. 1002–1006, Feb. 2014.

[8] N. G. Alexopoulos, "Integrated-circuit structures on anisotropic substrates," *IEEE Trans. Microw. Theory Techn.*, vol. 33, no. 10, pp. 847–881, Oct. 1985.

[9] B. Ivsic, Z. Sipus, and S. Hrabar, "Analysis of uniaxial multilayer cylinders used for invisible cloak realization," *IEEE Trans. Antennas Propag.*, vol. 57, no. 5, pp. 1521–1527, May 2009.

[10] C. Xiong, W. H. P. Pernice, and H. X. Tang, "Low-loss, silicon integrated, aluminum nitride photonic circuits and their use for electro-optic signal processing," *Nano Lett.*, vol. 12, no. 7, pp. 3562–3568, Jul. 2012.

[11] R. D. Graglia, P. L. E. Uslenghi, and R. S. Zich, "Moment method with isoparametric elements for three-dimensional anisotropic scatterers," *Proc. IEEE*, vol. 77, no. 5, pp. 750–760, May 1989.

[12] G. Kobidze and B. Shanker, "Integral equation based analysis of scattering from 3-D inhomogeneous anisotropic bodies," *IEEE Trans. Antennas Propag.*, vol. 52, no. 10, pp. 2650–2658, Oct. 2004.

[13] C. Forestiere, G. Miano, G. Rubinacci, A. Tamburrino, L. Udpa, and S. Ventre, "A frequency stable volume integral equation method for anisotropic scatterers," *IEEE Trans. Antennas Propag.*, vol. 65, no. 3, pp. 1224–1235, Mar. 2017.

[14] M. S. Tong, Y. Q. Zhang, R. P. Chen, and C. X. Yang, "Fast solutions of volume integral equations for electromagnetic scattering by large highly anisotropic objects," *IEEE Trans. Microw. Theory Techn.*, vol. 62, no. 7, pp. 1429–1436, Jul. 2014.

[15] G. P. Zouros and G. C. Kokkorakis, "Electromagnetic scattering by a general rotationally symmetric inhomogeneous anisotropic sphere," *IEEE Trans. Microw. Theory Techn.*, vol. 63, no. 10, pp. 3054–3065, Oct. 2015.

[16] G. D. Kolezas and G. P. Zouros, "CFVIE formulation for EM scattering on inhomogeneous anisotropic–metallic objects," *IEEE Trans. Antennas Propag.*, vol. 65, no. 7, pp. 3788–3793, Jul. 2017.

[17] G. Mumcu, K. Sertel, and J. L. Volakis, "Surface integral equation solutions for modeling 3-D uniaxial media using closed-form dyadic green's functions," *IEEE Trans. Antennas Propag.*, vol. 56, no. 8, pp. 2381–2388, Aug. 2008.

[18] Y. Shi and C.-H. Liang, "Analysis of uniaxial media using Calderón-preconditioned single-source combined field integral equation," *IEEE Antennas Wireless Propag. Lett.*, vol. 13, pp. 491–494, 2014.

[19] J. Schneider and S. Hudson, "A finite-difference time-domain method applied to anisotropic material," *IEEE Trans. Antennas Propag.*, vol. 41, no. 7, pp. 994–999, Jul. 1993.

[20] X.-Q. Sheng and Z. Peng, "Analysis of scattering by large objects with off-diagonally anisotropic material using finite element-boundary integral-multilevel fast multipole algorithm," *IET Microw., Antennas Propag.*, vol. 4, no. 4, pp. 492–500, 2010.

[21] Y.-L. Geng, X.-B. Wu, L.-W. Li, and B.-R. Guan, "Mie scattering by a uniaxial anisotropic sphere," *Phys. Rev. E, Stat. Phys. Plasmas Fluids Relat. Interdiscip. Top.*, vol. 70, no. 5, Nov. 2004, Art. no. 056609.

[22] Y.-D. Kong, C.-B. Zhang, and Q.-X. Chu, "An optimized one-step leapfrog HIE-FDTD method with the artificial anisotropy parameters," *IEEE Trans. Antennas Propag.*, vol. 68, no. 2, pp. 1198–1203, Feb. 2020.

[23] Y. Hu, Y. Fang, D. Wang, Q. Zhan, R. Zhang, and Q. H. Liu, "The scattering of electromagnetic fields from anisotropic objects embedded in anisotropic multilayers," *IEEE Trans. Antennas Propag.*, vol. 67, no. 12, pp. 7561–7568, Dec. 2019.

[24] W. S. Weiglhofer, "Dyadic green's functions for general uniaxial media," *IEE Proc. H (Microw., Antennas Propag.)*, vol. 137, no. 1, pp. 5–10, Feb. 1990.

[25] W. S. Weiglhofer, "Analytic methods and free-space dyadic green's functions," *Radio Sci.*, vol. 28, no. 5, pp. 847–857, Sep. 1993.

[26] C. Hafner, *Generalized Multipole Technique for Computational Electromagnetics*. Norwood, MA, USA: Artech House, 1990.

[27] T. Wriedt, *Generalized Multipole Techniques for Electromagnetic and Light Scattering*, vol. 4. Amsterdam, The Netherlands: Elsevier, 1999.

[28] C. Hafner and N. Kuster, "Computations of electromagnetic fields by the multiple multipole method (generalized multipole technique)," *Radio Sci.*, vol. 26, no. 1, pp. 291–297, Jan. 1991.

[29] Y. A. Eremin and A. G. Sveshnikov, "The discrete source method for investigating three-dimensional electromagnetic scattering problems," *Electromagnetics*, vol. 13, no. 1, pp. 1–22, Jan. 1993.

[30] D. I. Kaklamani and H. T. Anastassiu, "Aspects of the method of auxiliary sources (MAS) in computational electromagnetics," *IEEE Antennas Propag. Mag.*, vol. 44, no. 3, pp. 48–64, Jun. 2002.

[31] Y. Leviatan and A. Boag, "Analysis of electromagnetic scattering from dielectric cylinders using a multifilament current model," *IEEE Trans. Antennas Propag.*, vol. 35, no. 10, pp. 1119–1127, Oct. 1987.

[32] N. B. Piller and O. J. F. Martin, "Extension of the generalized multipole technique to three-dimensional anisotropic scatterers," *Opt. Lett.*, vol. 23, no. 8, pp. 579–581, Apr. 1998.

[33] V. V. Varadan, A. Lakhtakia, and V. K. Varadan, "Scattering by three-dimensional anisotropic scatterers," *IEEE Trans. Antennas Propag.*, vol. 37, no. 6, pp. 800–802, Jun. 1989.

[34] M. A. Moharram and A. A. Kishk, "Electromagnetic scattering from two-dimensional arbitrary objects using random auxiliary sources," *IEEE Antennas Propag. Mag.*, vol. 57, no. 1, pp. 204–216, Feb. 2015.

[35] M. A. Moharram and A. A. Kishk, "Efficient electromagnetic scattering computation using the random auxiliary sources method for multiple composite 3-D arbitrary objects," *IEEE Trans. Antennas Propag.*, vol. 63, no. 8, pp. 3621–3633, Aug. 2015.

[36] M. A. M. Hassan and A. A. Kishk, "Solutions for general-purpose electromagnetic problems using the random auxiliary sources method," *IEEE Trans. Antennas Propag.*, vol. 66, no. 4, pp. 1947–1956, Apr. 2018.

[37] J. Krupka, R. G. Geyer, M. Kuhn, and J. H. Hinken, "Dielectric properties of single crystals of Al_2/O_3, L_aAlO_3, $NdGaO_3$, $SrTiO_3$, and M_gO at cryogenic temperatures," *IEEE Trans. Microw. Theory Tech.*, vol. 42, no. 10, pp. 1886–1890, Oct. 1994.

[38] R. E. Collin, "A simple artificial anisotropic dielectric medium," *IEEE Trans. Microw. Theory Techn.*, vol. 6, no. 2, pp. 206–209, Apr. 1958.

[39] A. Shahvarpour, C. Caloz, and A. Alvarez-Melcon, "Broadband and low-beam squint leaky wave radiation from a uniaxially anisotropic grounded slab," *Radio Sci.*, vol. 46, no. 4, pp. 1–13, Aug. 2011.

[40] C. L. Holloway, M. S. Sarto, and M. Johansson, "Analyzing carbon-fiber composite materials with equivalent-layer models," *IEEE Trans. Electromagn. Compat.*, vol. 47, no. 4, pp. 833–844, Nov. 2005.

[41] T. C. Choy, *Effective Medium Theory: Principles And Applications*. Oxford, U.K.: Oxford Univ. Press, 2015, vol. 165.

[42] Y. Leviatan, A. Boag, and A. Boag, "Generalized formulations for electromagnetic scattering from perfectly conducting and homogeneous material bodies-theory and numerical solution," *IEEE Trans. Antennas Propag.*, vol. 36, no. 12, pp. 1722–1734, Dec. 1988.

[43] S. Rao, D. Wilton, and A. Glisson, "Electromagnetic scattering by surfaces of arbitrary shape," *IEEE Trans. Antennas Propag.*, vol. 30, no. 3, pp. 409–418, May 1982.

[44] *ALTAIR HyperWorks, Altair Feko(Version 2018)*. [Online]. Available: https://altairhyperworks.com/product/FEKO

[45] Computer Simulation Technology. *CST Studio Suite 2018*. [Online]. Available: https://www.3ds.com/products-services/simulia/products/cst-studio-suite

[46] Z.-S. Wu, Q.-K. Yuan, Y. Peng, and Z.-J. Li, "Internal and external electromagnetic fields for on-axis Gaussian beam scattering from a uniaxial anisotropic sphere," *J. Opt. Soc. Amer. A, Opt. Image Sci.*, vol. 26, no. 8, pp. 1778–1787, Aug. 2009.

[47] MathWorks. *MATLAB R2017b*. [Online]. Available: https://www.mathworks.com/

[48] H. T. Anastassiu, D. I. Kaklamani, D. P. Economou, and O. Breinbjerg, "Electromagnetic scattering analysis of coated conductors with edges using the method of auxiliary sources (MAS) in conjunction with the standard impedance boundary condition (SIBC)," *IEEE Trans. Antennas Propag.*, vol. 50, no. 1, pp. 59–66, Jan. 2002.

[49] K. Wang, J.-J. Laurin, and K. Wu, "Two-dimensional scattering from homogenous anisotropic cylinders using a multifilament current method," *IEEE Trans. Antennas Propag.*, early access, Jan. 9, 2020, doi: 10.1109/TAP.2020.2963908.

KAI WANG (Member, IEEE) received the B.Sc. degree from Anhui University, Hefei, China, in 2012, the M.Sc. degree from the South China University of Technology, Guangzhou, China, in 2015, and the Ph.D. degree from Polytechnique Montreal, Montreal, QC, Canada, in 2019.

He was a Research Assistant with the University of Macau, Macau, China, in 2014, and the South University of Science and Technology of China, Shenzhen, China, in 2015, where he conducted research on microwave balanced filters and filtering antennas, respectively. Since November 2019, he joined Pengcheng Laboratory, Shenzhen, as a Postdoctoral Fellow, where he is currently working on real-time millimeter and terahertz waves imaging techniques. His current research interests include imaging techniques, computational electromagnetics, leaky-wave antenna, dielectric resonator antenna, and planar microwave filter design. He has been formally nominated for the Best Ph.D. Thesis Award of University of Montreal, in 2020.

JEAN-JACQUES LAURIN (Senior Member, IEEE) received the B.Eng. degree in engineering physics from the École Polytechnique de Montréal, Montreal, QC, Canada, in 1983, and the M.A.Sc. and Ph.D. degrees in electrical engineering from the University of Toronto, Toronto, ON, Canada, in 1986 and 1991, respectively. In 1991, he joined the Poly-Grames Research Centre, École Polytechnique de Montréal, where he is currently a Professor. He is also the Co-Director of the Center for Systems, Technologies, and Applications for Radiofrequency and Communications (STARaCom), a strategic research cluster in QC.

QINGFENG ZHANG (Senior Member, IEEE) received the B.E. degree from the University of Science and Technology of China (USTC), Hefei, China, in 2007, and the Ph.D. degree from Nanyang Technological University, Singapore, in 2011, all in electrical engineering.

From June 2011 to December 2013, he was with the Poly-Grames Research Center, École Polytechnique de Montréal, Montreal, Canada, as a Postdoctoral Fellow. Since January 2014, he has been an Assistant Professor with the Southern University of Science and Technology, Shenzhen, China, where he is currently a Tenured Associate Professor, the Deputy Head of the Electronics and Electrical Engineering Department, and the Director of Shenzhen Engineering Center for Electromagnetic Nondestructive Detection. His research interests are largely in emerging novel electromagnetic technologies, where he has a special interest in dispersion engineering at microwave and millimeter-wave frequencies. He is a member of IET, ACES, and CIE. He has served as the TPC members of various international conferences, and also served in the review board of numerous journals in electromagnetics. He was a recipient of the URSI Young Scientist Award and the ACES Young Scientist Award, in 2018. He is also the Vice Chair of the IEEE Antennas and Propagation Society Shenzhen Chapter. He was the Publication Chair of 2016 IEEE ICCS, the Local Organization Committee Co-Chair of 2017 IEEE EDAPS, the TPC Co-Chair of Track 9 (Passive ICs and Active Antennas) in 2018 IEEE ICTA, and the Track Chair of 2019 ComComAp. He has served as an Associate Editor for IEEE Access and a Lead Guest Editor for the *International Journal of Antennas and Propagation*, from 2014 to 2015.

QINYU ZHANG (Senior Member, IEEE) received the bachelor's degree in communication engineering from the Harbin Institute of Technology (HIT), in 1994, and the Ph.D. degree in biomedical and electrical engineering from the University of Tokushima, Japan, in 2003. From 1999 to 2003, he was an Assistant Professor with the University of Tokushima. From 2003 to 2005, he was an Associate Professor with the Shenzhen Graduate School, HIT, where he was also the Founding Director of the Communication Engineering Research Center, School of Electronic and Information Engineering. Since 2005, he has been a Full Professor and the Dean of the EIE School, HIT. His research interests include aerospace communications and networks, wireless communications and networks, cognitive radios, signal processing, and biomedical engineering. He has been a TPC Member of INFOCOM, ICC, GLOBECOM, WCNC, and other flagship conferences in communications. He received three scientific and technological awards from governments and received the National Science Fund for Distinguished Young Scholars, the Young and Middle-Aged Leading Scientist of China, and the Chinese New Century Excellent Talents in University. He was the TPC Co-Chair of the IEEE/CIC ICCC 15, the Symposium Co-Chair of the IEEE VTC 16 Spring, the Associate Chair of Finance of ICMMT 12, and the Symposium Co-Chair of CHINACOM 11. He was the Founding Chair of the IEEE Communications Society Shenzhen Chapter. He is on the Editorial Board of some academic journals, such as the *Journal on Communications*, the *KSII Transactions on Internet and Information Systems*, and *Science China: Information Sciences*.

KE WU (Fellow, IEEE) received the B.Sc. degree (Hons.) in radio engineering from the Nanjing Institute of Technology (now Southeast University), China, in 1982, the D.E.A. degree (Hons.) in optics, optoelectronics, and microwave engineering from the Institut National Polytechnique de Grenoble (INPG), in 1984, and the Ph.D. degree (Hons.) in optics, optoelectronics, and microwave engineering from the University of Grenoble, France, in 1987.

He is currently a Professor of electrical engineering and the NSERC-Huawei Industrial Research Chair in future wireless technologies with the Polytechnique Montréal (University of Montreal), QC, Canada. He has been the Director of the Poly-Grames Research Center. He was the Founding Director of the Center for Radiofrequency Electronics Research of Quebec (Regroupement stratégique of FRQNT) and the Tier-I Canada Research Chair in RF and millimeter-wave engineering. He is also with the School of Information Science and Engineering, Ningbo University, on leave from his home institution, leading a special 5G and future wireless research program there. He has held guest, visiting, and honorary professorships with many universities around the world. He has authored or coauthored over 1200 refereed articles and a number of books/book chapters. He has filed more than 50 patents. His current research interests include substrate integrated circuits and systems, antenna arrays, field theory and joint field/circuit modeling, ultrafast interconnects, wireless power transmission and harvesting, and MHz-through-THz technologies and transceivers for wireless sensors and systems as well as biomedical applications. He is also interested in the modeling and design of microwave and terahertz photonic circuits and systems.

Dr. Wu is a Fellow of the Canadian Academy of Engineering (CAE) and the Royal Society of Canada (The Canadian Academy of the Sciences and Humanities). He is also a member of the Electromagnetics Academy, Sigma Xi, URSI, and IEEE-Eta Kappa Nu (IEEE-HKN). He is the inaugural representative of North America as a member of the European Microwave Association (EuMA) General Assembly. He was a recipient of many awards and prizes, including the first IEEE MTT-S Outstanding Young Engineer Award, the 2004 Fessenden Medal of the IEEE Canada, the 2009 Thomas W. Eadie Medal of the Royal Society of Canada, the Queen Elizabeth II Diamond Jubilee Medal in 2013, the 2013 FCCP Education Foundation Award of Merit, the 2014 IEEE MTT-S Microwave Application Award, the 2014 Marie-Victorin Prize (Prix du Quebec—the highest distinction of Quebec in the natural sciences and engineering), the 2015 Prix d'Excellence en Recherche et Innovation of Polytechnique Montreal, and the 2015 IEEE Montreal Section Gold Medal of Achievement. He has held key positions in and has served on various panels and international committees, including the Chair of Technical Program Committees, International Steering Committees, and international conferences/symposia. In particular, he was the General Chair of the 2012 IEEE Microwave Theory and Techniques (IEEE MTT-S) International Microwave Symposium (IMS). He has served on the Editorial/Review Boards for many technical journals, transactions, proceedings, and letters as well as scientific encyclopedia, including an Editor and a Guest Editor. He was the Chair of the joint IEEE Montreal chapters of MTT-S/AP-S/LEOS and then the restructured IEEE MTT-S Montreal Chapter, Canada. He has served on the IEEE MTT-S and Administrative Committee (AdCom) as the Chair of the IEEE MTT-S Transnational Committee, Member and Geographic Activities (MGA) Committee, Technical Coordinating Committee (TCC) and 2016 IEEE MTT-S President among many other AdCom functions. He was an IEEE MTT-S Distinguished Microwave Lecturer, from 2009 to 2011.